J. Fluid Mech. (2003), *vol.* 481, *pp.* 37–66.
DOI: 10.1017/S0022112002003658 Printed in the United Kingdom

On axisymmetric rotating gravity currents: two-layer shallow-water and numerical solutions

By M. UNGARISH AND T. ZEMACH

Computer Science Department, Technion – Israel Institute of Technology, Haifa 32000, Israel

(Received 11 February 2002 and in revised form 27 June 2002)

Axisymmetric gravity currents released from behind a lock over a solid horizontal bottom in a system rotating about a vertical axis are investigated. The major parameters are $\mathscr{C}$, the ratio of Coriolis to inertia forces, and H, the ratio of the total height of the ambient fluid into which propagation occurs to the initial height of the dense fluid inside the lock. We focus attention on the small $\mathscr{C}$, almost inviscid case in which a significant radius of propagation is obtained. A two-layer shallow-water inviscid approximation is developed and it is shown that the angular velocities in the upper and lower layers are coupled by simple relationships which can be used to simplify both the time-dependent and the steady-state lens solutions. However, the major features predicted by the two-layer model differ only slightly from these obtained with a one-layer model. Finite-difference solutions of the full Navier–Stokes equations are also presented and compared with the shallow-water approximations.

1. Introduction

Gravity currents are formed by a fluid flowing primarily horizontally under the influence of gravity into another fluid of a different density. The typical problem considers the instantaneous release of a constant volume of dense fluid from behind a lock into a large reservoir of ambient fluid, above an impermeable horizontal boundary. Currents may propagate in either a two-dimensional (rectangular) or axisymmetric (cylindrical) geometry configuration. The axisymmetric current is more complex and less understood than the rectangular counterpart. Another important effect which accompanies the axisymmetric current in many practical industrial and environmental circumstances is the rotation of the frame in which propagation takes place. For example, Flierl (1979) and Csanady (1979) suggested Coriolis-buoyancy balance models for explaining the behaviour of typical Gulf Stream 'rings' of radius and thickness of about 100 km and 1 km, respectively. On the other hand, related laboratory experiments concern 'eddies' whose magnitude is several centimetres in the common case (Griffiths & Linden 1981; Nof & Simon 1987) and up to several metres in special facilities like the Coriolis LEGI at Grenoble (Hallworth, Huppert & Ungarish 2001).

The purpose of our investigation is to extend the knowledge about the motion of high-Reynolds-number homogeneous gravity currents of finite volume in an axisymmetric geometry, in particular with background rotation. We shall use both shallow-water approximations and numerical solutions of the Navier–Stokes equations.

Analytical investigations of axisymmetric gravity currents of fixed volume in a rotating frame have been performed by Ungarish & Huppert (1998) for the one-layer

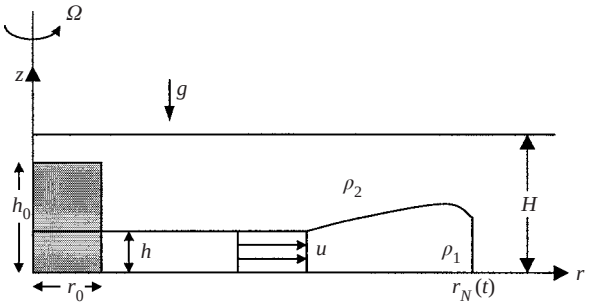

FIGURE 1. Schematic description of the system: z is the axis of symmetry. The grey region sketches the current at $t = 0$. The initial densities in the ambient and dense fluid are ρ_a $(= \rho_2)$ and ρ_d $(= \rho_1)$.

shallow-water model. For this model, the appropriately defined Reynolds number is assumed to be large and hence viscous effects need not be incorporated, the shallow-water approximation is used to simplify the equations of motion and the purely hydrostatic balance (i.e. no relative motion of the fluid in the rotating system) is assumed for the ambient fluid domain. In the present work, we extend the analysis to a two-layer model. This means that the assumption of pure hydrostatic balance in the ambient fluid is relaxed.

The system under consideration is sketched in figure 1: a layer of ambient fluid of density ρ_a above a solid horizontal surface $z = 0$, is in solid-body rotation with angular velocity Ω about the vertical axis of symmetry. The upper boundary is open to the atmosphere. At time $t = 0$, a fixed-volume of co-rotating denser fluid of density ρ_d, initially in a cylinder of height h_0 and radius r_0, is released into the ambient fluid. We denote by H the ratio of the total height of the fluids in the system to h_0 of the lock (we neglect the small curvature of the free surface, as justified later); we are interested in cases with $H \geqslant 1$, i.e. the dense fluid behind the lock is, initially and after release, shallower than the ambient fluid.

An axisymmetric current starts to spread radially at $t = 0$. The driving mechanism for propagation is provided by the pressure head at the nose of the dense fluid and hence the characteristic radial velocity is $(g'h_0)^{1/2}$; here, the reduced gravity is defined by

$$g' = \epsilon\, g, \tag{1.1}$$

where

$$\epsilon = \frac{\rho_d}{\rho_a} - 1. \tag{1.2}$$

On the other hand, in a rotating system the gravity-driven propagation is modified and eventually suppressed by the Coriolis-centrifugal effects, reflected by the dimensionless parameter

$$\mathscr{C} = \frac{\Omega r_0}{(g'h_0)^{1/2}} = \frac{1}{Ro}, \tag{1.3}$$

which expresses the ratio of the azimuthal velocity Ωr_0 to the inertial velocity $(g'h_0)^{1/2}$ and can be defined as the inverse of the formal Rossby number Ro. The Coriolis-centrifugal effects remain after the decay of the inertial processes. For this reason (i)

Coriolis effects† may produce significant differences from non-rotating currents even for very small values of $\mathscr{C}$, and (ii) the dense fluid may attain a quasi-steady lens shape, dominated by a Coriolis-pressure balance, when the radial velocity decays, in contrast with non-rotating currents which become dominated by viscous forces at large times.

Steady lens structures have been studied by Griffiths & Linden (1981), Nof & Simon (1987), Dewar & Killworth (1990), Choboter & Swaters (2000) and others, mostly for large values of the parameter $\mathscr{C}$ and under the assumption that the ambient fluid is motionless (in the rotating system). We shall briefly reconsider this topic and present some improved results.

The propagation of gravity currents is conveniently approximated by the shallow-water (SW) theory. For the rotating current, only the one-layer model was studied (see Ungarish & Huppert 1998; Hallworth *et al.* 2001). The one-layer model assumes that no motion takes place in the ambient. This assumption can be justified for a current covered by a relatively very thick layer of ambient, i.e. in the limit $H = \infty$. However, this limit is unrealistic in many practical, experimental and computational circumstances. Our task here is to incorporate the ambient fluid effects into the modelling of that flow and to understand their major influence. In the SW modelling, the appropriate equations for the ambient fluid layer must be added to the previously studied system and the interaction terms between the layers must be reformulated.

For the non-rotating rectangular geometry case, two-layer SW models have been investigated (see Rottman & Simpson 1983 and Klemp, Rotunno & Skamarock 1994). A useful conclusion is that the two-layer model in the non-rotating case can be reduced to the solution of PDEs for only one layer. However, the proper incorporation of the angular momentum equations in the two-layer model requires a special extension, as shown later. The simulation of the gravity current motion by the SW formulation requires, in general, a numerical solution, but the necessary code is obtained by a relatively modest programming effort, and the typical run takes about 1 CPU min on a regular workstation. Moreover, the interpretation of the results is simple.

On the other hand, in our code of finite difference numerical solution of the Navier–Stokes equations (NS approach), the domain of computation is a cylinder of height H in which both fluids move subject to global boundary conditions. Therefore, the motion of the ambient is an intrinsic part of this solution. The disadvantage of this method is the complexity of the necessary code and programming task, the high computational price (many CPU hours, even on powerful computers), and the subsequent efforts required to process the detailed resulting data.

The paper is organized as follows. The Navier–Stokes formulation is given in § 2 and the corresponding numerical solution is discussed in § 3. In § 4, the shallow-water approximations and the appropriate boundary conditions, with emphasis on the two-layer angular momentum balances, are developed. The steady lens are also discussed. Results of the time-dependent flow as predicted by the SW and NS approaches are presented and compared in § 5. Some concluding remarks are made in § 6.

2. Formulation

We use a cylindrical coordinate system rotating with angular velocity Ω about the vertical axis of symmetry z. The velocity vector corresponding to the coordinates

† For brevity, we mainly use 'Coriolis' to refer to the Coriolis and centrifugal effects in the rotating system.

$\{r, \theta, z\}$ is denoted by $\boldsymbol{v} = \{u, v, w\}$; the (relative) angular velocity is defined by

$$\omega = v/r. \tag{2.1}$$

We assume axial symmetry.

It is convenient to replace the dimensional variables, denoted here by asterisks, with dimensionless counterparts, for which no special notation is used, scaled by the following relationships:

$$\{r^*, z^*, t^*, u^*, v^*, w^*, \omega^*, p^*\} = \left\{r_0 r, h_0 z, Tt, Uu, \Omega r_0 v, \left(\frac{h_0}{r_0}\right) Uw, \Omega\omega, \rho_a U^2 p\right\}, \tag{2.2}$$

where

$$U = (h_0 g')^{1/2}, \quad T = \frac{r_0}{(h_0 g')^{1/2}}. \tag{2.3}$$

The dimensional reference quantities are as follows: h_0 is the initial height of the current, r_0 its initial radius, Ω is the angular velocity of the system, g' is the reduced gravity, U and T are the typical velocity and time of propagation of the front (nose) in a non-rotating gravity-current problem. The variable p represents the reduced pressure (in dimensional form, the reduction is by $\rho_a(0.5\Omega^2 r^{*2} - gz^*)$). The scaling (2.2)–(2.3) is advantageous in particular for the shallow-water approach to the flow field; the approximate equations are straightforwardly developed and, more important, the initial aspect ratio h_0/r_0 is eliminated from the resulting formulation (see Ungarish & Huppert 1999).

We introduce the dimensionless density function $\phi(\boldsymbol{r}, t)$ defined by

$$\rho(\boldsymbol{r}, t) = \rho_a[1 + \epsilon\,\phi(\boldsymbol{r}, t)]. \tag{2.4}$$

where, again, ρ_a is the dimensional density of the ambient. We expect $0 \leqslant \phi \leqslant 1$, with $\phi = 1$ in the 'pure' dense fluid domain and $\phi = 0$ in the 'pure' ambient fluid domain.

The dimensionless governing equations are as follows.

Continuity of volume

$$\nabla \cdot \boldsymbol{v} = 0. \tag{2.5}$$

Momentum balance in the radial (horizontal), azimuthal and axial (vertical) directions

$$\frac{\mathrm{D}u}{\mathrm{D}t} - 2\mathscr{C}^2 v - \mathscr{C}^2 \frac{v^2}{r} = \frac{1}{1+\epsilon\,\phi}\left[-\frac{\partial p}{\partial r} + \phi\epsilon\,\mathscr{C}^2 r + \frac{1}{Re}\nabla_c^2 u\right], \tag{2.6}$$

$$\frac{\mathrm{D}v}{\mathrm{D}t} + \frac{uv}{r} + 2u = \frac{1}{1+\epsilon\,\phi}\left[\frac{1}{Re}\nabla_c^2 v\right], \tag{2.7}$$

$$\left(\frac{h_0}{r_0}\right)^2 \frac{\mathrm{D}w}{\mathrm{D}t} = \frac{1}{1+\epsilon\,\phi}\left[-\frac{\partial p}{\partial z} - \phi + \frac{1}{Re}\left(\frac{h_0}{r_0}\right)^2 \nabla^2 w\right]. \tag{2.8}$$

Dense component transport

$$\frac{\mathrm{D}\phi}{\mathrm{D}t} = \mathscr{D}\nabla^2\phi. \tag{2.9}$$

We used the notation

$$\nabla^2 f = \frac{1}{r}\frac{\partial}{\partial r} r \frac{\partial f}{\partial r} + \left(\frac{h_0}{r_0}\right)^{-2} \frac{\partial^2 f}{\partial z^2}, \quad \nabla_c^2 f = \nabla^2 f - \frac{f}{r^2}. \tag{2.10}$$

The relevant dimensionless parameters in these equations, in addition to the reduced density difference ϵ and the initial aspect ratio h_0/r_0, are the Coriolis to inertia ratio parameter

$$\mathscr{C} = \frac{\Omega r_0}{(g'h_0)^{1/2}}, \tag{2.11}$$

the Reynolds number

$$Re = (g'h_0)^{1/2} r_0 \rho_a / \mu, \tag{2.12}$$

and the dimensionless diffusion coefficient $\mathscr{D} = 1/Pe = 1/(\sigma Re)$ where Pe and σ are the Péclet and Schmidt numbers, and μ is the dynamic viscosity, assumed equal in both fluids.

We are interested in flows with large values of Re, moderately small $\mathscr{C}$, small ϵ and very small $\mathscr{D}$. The typical physical value of $\mathscr{D}$ is negligibly small (recall that $\sigma \gg 1$ for saline solutions in water), but here a non-vanishing $\mathscr{D}$ is used as an artificial diffusion coefficient for numerical smoothing.

The parameter $\mathscr{C}$, which typifies the ratio of the Coriolis to inertia terms, may be regarded as the inverse of a Rossby number, Ro; in this context, a flow field with a small $\mathscr{C}$ means one with a large Ro. The Ekman number can be defined in terms of the previous parameters as

$$\mathscr{E} = \frac{\mu}{\Omega h_0^2 \rho_a} = \left[\left(\frac{h_0}{r_0} \right)^2 \mathscr{C} Re \right]^{-1}, \tag{2.13}$$

and is assumed small; $\mathscr{E}^{1/2}$ is the typical (dimensionless) thickness of the rotational horizontal viscous layers which develop after about one revolution of the system.

The parameter (h_0/r_0) represents the 'shallowness' of the current, and is assumed small. In the axially symmetric lock-release problem considered here, two more geometric parameters appear: the initial ratio of the total height of the ambient fluid to the height of the dense fluid in the lock (or the dimensionless total height of the fluids), H, and the initial length ratio (or the dimensionless radius of the container), r_w. The former may assume various values (but here at least 1, and typically large), and the latter is assumed sufficiently large for not interfering with the motion of the current for the time period of interest.

For a physical reference system, we may consider the following laboratory setting: in a tank with pure water of height 20 cm and diameter 1 m, we release a saline current of $h_0 = 5$ cm, $r_0 = 10$ cm and $g' = 10\,\mathrm{cm^2\,s^{-1}}$, and the system rotates with $\Omega = 1$ r.p.m. For this case, $\mathscr{C} = 0.15$, $Re = 7 \times 10^3$, $\epsilon = 10^{-2}$, $\mathscr{D} = 2 \times 10^{-7}$, $H = 4$ and $r_w = 5$. The parameters $\mathscr{C}$ and H can be varied easily.

The initial conditions at $t = 0$ are

$$\boldsymbol{v} = 0 \quad (0 \leqslant r \leqslant r_w, \quad 0 \leqslant z \leqslant H), \tag{2.14}$$

$$\phi = \begin{cases} 1 & (0 \leqslant r \leqslant 1, \quad 0 \leqslant z \leqslant 1), \\ 0 & \text{elsewhere.} \end{cases} \tag{2.15}$$

The boundary conditions for $t \geqslant 0$ are

$$\boldsymbol{v} = 0 \quad \text{(on the bottom and sidewalls)}, \tag{2.16}$$

$$w = 0 \quad \text{and no shear} \quad (z = H), \tag{2.17}$$

$$u = 0 \quad \text{and regularity} \quad (r = 0), \tag{2.18}$$

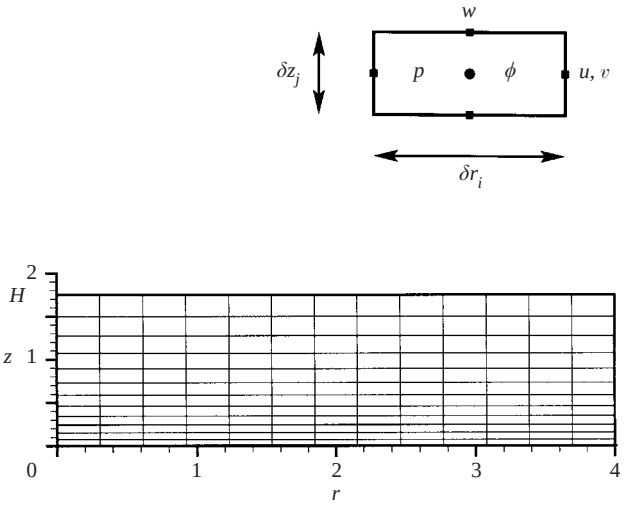

FIGURE 2. Sketch of numerical grid ($r_w = 4, H = 1.75$), and the details of one cell. The centre of the computational cell is denoted by (i, j), corresponding to the position r_i, z_j, $(1 \leqslant i \leqslant il,\ 1 \leqslant j \leqslant jl)$.

and

$$\hat{\boldsymbol{n}} \cdot \nabla \phi = 0 \quad \text{(on all boundaries)}. \tag{2.19}$$

These conditions contain some simplifications, in particular (2.17) which is the frictionless 'rigid lid' approximation for the free surface. The initial interfaces (between the ambient and dense fluids and also the free surface of ambient fluid) deviate from the horizontal by an amount $0.5\epsilon \mathscr{C}^2 r^2$. The free surface will also have an additional $O(\epsilon)$ deformation during the flow. Neglecting these departures from the horizontal is justified for the small values of ϵ and $\mathscr{C}^2$ used in this investigation. In addition, we assume that the lock is removed instantaneously and without any perturbation to the fluid. (In real situations, such as laboratory experiments, the lock lifting is expected to introduce a small delay in the initial motion which is a source of discrepancy between theory and measurements.)

The two-dimensional version of the foregoing formulation in a rectangular non-rotating x, z-coordinate system can be obtained as follows: (i) set $v \equiv 0$, $\mathscr{C} = 0$, and replace r with x; (ii) delete the curvature terms, and (iii) change the regularity boundary condition on the axis, (2.18), with no-slip.

3. Navier–Stokes numerical simulation (NS) approach

The foregoing system of equations and boundary conditions, subject to the axial-symmetry assumption, is solved by a time-marching finite-difference discretization method. The details are described in Hallworth *et al.* (2001). Briefly, the method is based on forward-time discretization of the velocity components, with implicit Coriolis and pressure terms. The continuity equation for the new velocity field yields an elliptic equation for the new pressure field.

The spatial discretization is performed on a staggered grid with il radial intervals and jl axial intervals as sketched in figure 2. The variables p and ϕ are defined at mid-cell position denoted (i, j); u and v are both defined at the positions $(i \pm \frac{1}{2}, j)$ (to allow straightforward implementation of the Coriolis coupling) and w is defined at

$(i, j \pm \frac{1}{2})$. Both the r and z grid coordinates are stretched by simple mapping functions $r(R)$ and $z(Z)$. The grids $R_i = (i + \frac{1}{2})\delta R$ and $Z_j = (j + \frac{1}{2})\delta Z$ are uniform in the domain $(0 \leqslant R \leqslant r_w, \quad 0 \leqslant Z \leqslant H)$ with intervals $\delta R = r_w/il$, and $\delta Z = H/jl$. The truncation error is $O(\delta R^2 + \delta Z^2)$. Dummy cells were added for easy implementation of boundary conditions. An illustration of the finite-difference approximation approach is

$$\left(\frac{1}{r}\frac{\partial}{\partial r} r \frac{1}{1+\epsilon\,\phi}\frac{\partial p}{\partial r}\right)_{r_i, z_j} \approx \frac{1}{r_i}\frac{1}{r_i' \delta R}\left(Y_{i+1/2,\,j} - Y_{i-1/2,\,j}\right), \tag{3.1}$$

where

$$Y_{i+1/2,\,j} = r_{i+1/2}\frac{1}{1+\epsilon\,\phi_{i+1/2,\,j}}\frac{1}{r'_{i+1/2}\delta R}(p_{i+1,\,j} - p_{i,\,j}), \tag{3.2}$$

and r_i' is the derivative of $r(R)$ at R_i (substituting $i-1$ in place of i yields $Y_{i-1/2,\,j}$).

This method of central differences was employed for all terms, except for the advection terms in the ϕ transport equation (2.9). The interface between the pure and the dense fluids is represented by a sharp gradient in ϕ which may cause strong oscillations in numerical finite-difference schemes. To avoid this spurious effect, in the solution of (2.9) we implemented MacCormack's explicit method, see Anderson, Tannehill & Pletcher (1984), i.e. we used at each time step a predictor–corrector relationship which combines forward and backward differences of the advection terms in two half-steps. Comparisons of computed results confirmed the smoothing effect of this approach.

The combination of the foregoing time and space discretization are the core of the computer code used in this work. For each time step, the discretized form of the Poisson equation for the 'new' pressure variables $p^+_{i,j}, 1 \leqslant i \leqslant il, 1 \leqslant j \leqslant jl$ must be solved. This yields, after the implementation of the boundary conditions, a block tri-diagonal linear system which was solved by a bi-conjugate gradient iterative algorithm (see Press *et al.* 1992). The computations use real-8 variables. The typical grid has $il = 200$ constant radial intervals and $jl = 150$ slightly stretched axial intervals and the typical time step was $\delta t = 10^{-3}$.

The choice of the numerical grid parameters was motivated by the compromise between accuracy considerations and computational limitations. Essentially, the mesh intervals are considerably smaller than the expected typical corresponding geometrical dimensions of the simulated current (e.g. the length of the 'head', the average thickness, and even the Ekman layer thickness (estimated as $3\mathscr{E}^{1/2}$). We therefore expect that the numerical results provide an acceptable simulation of an observable gravity-current process, at least during the initial period. Eventually, when the current becomes thin (say, about 10 axial intervals) and the interface very irregular, the numerical errors may become significant and even dominant.

The major task was to simulate the rotating current for the time interval $t \approx 2\mathscr{C}^{-1}$ (in dimensional form, $\Omega t^* \approx 2$), during which the most significant effects of propagation and attainment of maximal spread are expected to take place.

For the simulation of two-dimensional rectangular non-rotating currents, a special version of the numerical code was also developed, as outlined in the last paragraph of the previous section, but the details will be presented elsewhere.

4. The inviscid shallow-water (SW) approximation

The following main simplifications are introduced. Let $r_N(t)$ denote the radius of the 'nose' of the dense fluid current. A sharp interface, $z = h(r, t), 0 \leqslant r \leqslant r_N(t)$, is

assumed to separate the fixed volume of dense fluid from the ambient. This defines an 'upper' layer whose variables are denoted by the the subscript 2, and a 'lower' layer, whose variables are denoted by the subscript 1 when necessary (when no subscript is given for an SW variable, we refer to the lower layer). The densities in the layers are assumed constant, $\rho_1 = \rho_d$ and $\rho_2 = \rho_a$, and hence the values of the density function, see (2.4), are $\phi_1 = 1$ and $\phi_2 = 0$.

We consider the limiting case when both $1/Re$ and h_0/r_0 are very small, and neglect all terms multiplied by these parameters in the momentum equations (2.6)–(2.8).

The axial momentum equation (2.8) reduces to the hydrostatic balance for both layers, and integration with respect to z and subject to continuity of pressure at the interface yields

$$p_1(r, z, t) = p_I(r, t) + [h(r, t) - z], \quad p_2(r, z, t) = p_I(r, t), \tag{4.1}$$

where $p_I(r, t)$ is the pressure at $z = h(r, t)$.

Next, the governing equations are z-averaged (separately in domains 1 and 2) and reduced to equations for the z-averaged variables $u_i(r, t)$ and $v_i(r, t)$ $(i = 1, 2)$; $h_1(r, t)$ and $h_2(r, t)$ denote the thickness of the domains. Evidently, $h_1 = h$, the locus of the interface.

Hereinafter, in the spirit of the 'shallow-water' framework, the z-averaged variables u_i and v_i are considered as functions of r and t only. The resulting equations for these variables are presented below, in dimensionless form.

4.1. *The governing SW equations*

The full partial-differential system, in conservation form, can be written as

$$\frac{\partial h_1}{\partial t} + \frac{\partial}{\partial r}(u_1 h_1) = -\frac{u_1 h_1}{r}, \tag{4.2}$$

$$\frac{\partial h_2}{\partial t} + \frac{\partial}{\partial r}(u_2 h_2) = -\frac{u_2 h_2}{r}, \tag{4.3}$$

$$\frac{\partial}{\partial t}(u_1 h_1) + \frac{\partial}{\partial r}\left(u_1^2 h_1 + \tfrac{1}{2} h_1^2\right) = -\frac{u_1^2 h_1}{r} - h_1 \frac{1}{1+\epsilon}\frac{\partial p_I}{\partial r} + \mathscr{C}^2 v_1 h_1 \left(2 + \frac{v_1}{r}\right) + \mathscr{C}^2 \epsilon\, r h_1 \frac{1}{1+\epsilon}, \tag{4.4}$$

$$\frac{\partial}{\partial t}(u_2 h_2) + \frac{\partial}{\partial r}\left(u_2^2 h_2\right) = -\frac{u_2^2 h_2}{r} - h_2 \frac{\partial p_I}{\partial r} + \mathscr{C}^2 v_2 h_2 \left(2 + \frac{v_2}{r}\right), \tag{4.5}$$

$$\frac{\partial}{\partial t}(v_1 h_1) + \frac{\partial}{\partial r}(u_1 v_1 h_1) = -2 u_1 h_1 \left(1 + \frac{v_1}{r}\right), \tag{4.6}$$

$$\frac{\partial}{\partial t}(v_2 h_2) + \frac{\partial}{\partial r}(u_2 v_2 h_2) = -2 u_2 h_2 \left(1 + \frac{v_2}{r}\right). \tag{4.7}$$

On the right-hand sides of the radial momentum equations (4.4) and (4.5) we readily identify the curvature, pressure and Coriolis-centrifugal terms. However, (4.4) contains two additional terms: the last one on the left-hand side is the pressure contributed by the larger density of the fluid below the interface, and the last term on the right-hand side, which is actually negligible, represents an excess of centrifugal effects not

accounted for in the reduced pressure. The geometry and global continuity impose

$$h_1 + h_2 = H, \tag{4.8}$$

$$u_1 h_1 + u_2 h_2 = 0. \tag{4.9}$$

The number of partial differential equations required for obtaining the solution can be reduced. Obviously, the result of (4.3) can be obtained from (4.2), (4.8) and (4.9). Moreover, as shown by Rottman & Simpson (1983), upon elimination of p_I from (4.4)–(4.5) and using (4.8)–(4.9) to eliminate u_2 and h_2 subsequently, we can decouple the radial momentum equation of layer 1 from its counterpart of layer 2. It is therefore unnecessary to solve the latter equation, since u_2 can be obtained from (4.9). The decoupled radial momentum equation reads

$$\frac{\partial}{\partial t}(u_1 h_1) + \left[\frac{B}{A} + 1\right] u_1 \frac{\partial}{\partial r}(u_1 h_1) + \left[\frac{C}{A} h_1 - \frac{B}{A} u_1^2\right] \frac{\partial h_1}{\partial r} = h_1 \frac{E}{A} + h_1 \frac{D}{A} - \frac{u_1^2 h_1}{r}, \tag{4.10}$$

where

$$\left.\begin{aligned} A &= 1 + ka, \\ B &= 1 - ka \frac{H + h_1}{H - h_1}, \\ C &= 1 - k(1+a)^3 \frac{u_1^2}{H}, \\ D &= k \frac{H h_1}{(H - h_1)^2} \frac{u_1^2}{r}, \\ E &= \mathscr{C}^2 \left[v_1 \left(2 + \frac{v_1}{r}\right) - k v_2 \left(2 + \frac{v_2}{r}\right)\right], \end{aligned}\right\} \tag{4.11}$$

and

$$a = \frac{h_1}{H - h_1}, \qquad k = (1 + \epsilon)^{-1}. \tag{4.12}$$

Hereinafter, in the SW formulation, we invoke the Boussinesq approximation setting $\epsilon = 0$ (i.e. $k = 1$) in the coefficients (4.11)–(4.12).

The Coriolis-centrifugal influence in the radial momentum balance is represented by the term E in the right-hand side of (4.10).

The governing system has been reduced to contain the partial differential equations (4.2), (4.10) and (4.6)–(4.7), supplemented by the algebraic equations (4.8)–(4.9). We shall show in § 4.3 that additional reduction concerning the azimuthal motion can be performed, but it is convenient to consider first the initial and boundary conditions.

The characteristic form of the equations is presented in the Appendix. An inspection of (A 2) and (A 6)–(A 7) leads to the conclusion that the velocity of propagation of the characteristics is not influenced by the angular velocity; on the other hand, both the rotation and curvature contribute important source terms to the balance of h and u on the characteristics.

4.2. *The initial and boundary conditions*

The ambient is assumed unbounded in the radial direction, and hence no *a priori* limitation on the propagation of the current is imposed. Practically, however, the radial spread is restricted by the Coriolis effects, as discussed below, or by the viscous

shear which is bound to become dominant when the head becomes thin and slow (more precisely, when $u_N^* h_N^* \rho_a/\mu < 50$).

The initial aspect ratio condition, h_0/r_0, has been eliminated from the SW formulation as a result of the scaling (2.2)–(2.3).

The initial conditions are zero velocity, $h_1 = 1$ and $r_N = 1$ at $t = 0$.

The velocity boundary conditions for the above mentioned system are:

(i) No-flow and regularity at the centre

$$u_1 = 0, \quad \frac{\partial \omega_i}{\partial r} = 0 \quad (r = 0, \quad i = 1, 2), \tag{4.13}$$

where $\omega_i = v_i/r$.

(ii) Dynamic nose-front condition.

For the present hyperbolic system of governing equations, the nose of the dense fluid current is a shock discontinuity whose speed is provided by additional considerations. The consensus is that the nose of a realistic space- and time-dependent gravity current obeys a local quasi-steady correlation between the height h_N and the velocity u_N. The underlying theory for this correlation was developed by Benjamin (1968) (in a two-dimensional geometry): balance of flow force (momentum plus pressure) and volume continuity between the approaching and receding stream (with respect to the nose) in an inviscid fluid yield

$$u_N = Fr(h_N/H)(h_N)^{1/2}, \tag{4.14}$$

where the Froude 'number' Fr is an explicit function (equation (2.22) in that paper) and varies in a narrow range about 1. Experiments confirmed the qualitative behaviour of (4.14), but also indicated quantitative discrepancies with the function Fr of Benjamin (1968), which can be attributed to various small-scale effects such as viscous friction and mixing. This motivated attempts to introduce empirical modifications of the $Fr(h_N/H)$ function. Rottman & Simpson (1983) performed calculations, by the method of characteristics, of a current released from behind a lock in a rectangular geometry using the two-layer SW equations, closed by the front condition (4.14) with the Fr function derived by Benjamin (1968), but multiplied by an adjustable coefficient denoted β. They showed that fair agreement with experiments was obtained for $\beta = 1$, although the theoretical value is $\beta = \sqrt{2}$.

Huppert & Simpson (1980) suggested an empirical curve-fit correlation (derived for two-dimensional non-rotating currents) which is simpler and seems to provide a wider agreement with available data, as follows,

$$Fr = \begin{cases} 1.19 & (0 \leqslant h_N/H \leqslant 0.0742), \\ 0.5 H^{1/3} h_N^{-1/3} & (0.0742 \leqslant h_N/H \leqslant 1), \end{cases} \tag{4.15}$$

We shall use this correlation in the SW calculation in conjunction with (4.14), where h_N and u_N are the instantaneous values of h_1 and u_1 at $r_N(t)$.

Figure 3 displays the different formulae for Fr as a function of h_N/H. It is observed that (4.15) is bounded by the values tested by Rottman & Simpson (1983) for $0 < h_N/H < 0.6$. (We note in passing that the range $h_N/H > 0.6$ is spurious because it implies a velocity of the nose larger than that of the forward characteristic and, in any case, is outside the parameter range of this study.)

The use of (4.14)–(4.15) in axisymmetric configurations shows good agreements with experiments, see Hallworth *et al.* (2001), figure 4.

For a rotating axisymmetric current, $\mathscr{C} > 0$, to the best of our knowledge no detailed investigation on the nose condition has been performed. However, following

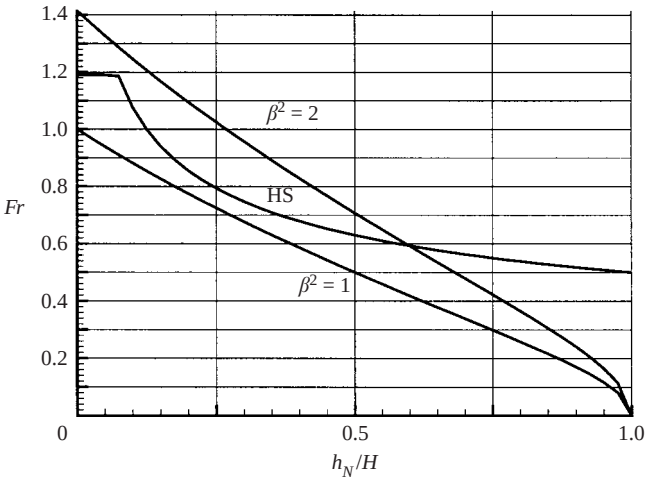

FIGURE 3. *Fr* as a function of h_N/H: the correlations of Rottman & Simpson for two values of β^2, and of Huppert & Simpson (HS) which is used in this work, equation (4.15).

Ungarish & Huppert (1998) and Hallworth *et al.* (2001), we argue that the force balance used in the derivation of the nose conditions by Benjamin (1968) requires an $O(\mathscr{C}^2)$ correction if a background rotation is present, and hence (4.14)–(4.15) may be used as a fair approximation in the present case, at least when $\mathscr{C}^2 \ll 1$. Indeed, Ungarish & Huppert (1998) and Hallworth *et al.* (2001) used this approximation for a one-layer model and obtained fair agreement with experiments. This conclusion turns out to be valid also for the two-layer model as shown in this work.

(iii) The lower-layer angular velocity nose condition.

The characteristic path and balance associated with the angular momentum equation of the lower layer are relatively simple, see (A 2) and (A 10), and identical with the one-layer case, cf. Ungarish & Huppert (1998). Integration along a pertinent characteristic attached to the nose yields

$$\omega_1(r = r_N) = -1 + \left(\frac{1}{r_N(t)}\right)^2. \tag{4.16}$$

(This result also expresses the conservation of potential vorticity in the lower layer, as discussed later.)

(iv) The upper-layer angular velocity nose condition.

From angular momentum and volume conservation considerations we obtain

$$\omega_2(r = r_N) = 0. \tag{4.17}$$

To derive this result, we considered the motion of the ambient fluid which flows inward from $r > 1$ to cover the lower-layer fluid which flows outward, see figure 4. We assume that the ambient fluid from the outside moves in axisymmetric shells, which means that a ring from a smaller radius is displaced before a ring of the ambient fluid located at larger radius, and that each ring conserves the appropriate angular momentum. Let $r_O(t)$ be the initial radius of the 'last' ring of fluid which moved in to take its place just above the nose of the lower layer, at $r = r_N(t)$. An inspection of the configuration, see figure 4 (as well as analytical volume balance calculations) proves that $r_O = r_N$, i.e. the 'last' ring of ambient fluid which is above the

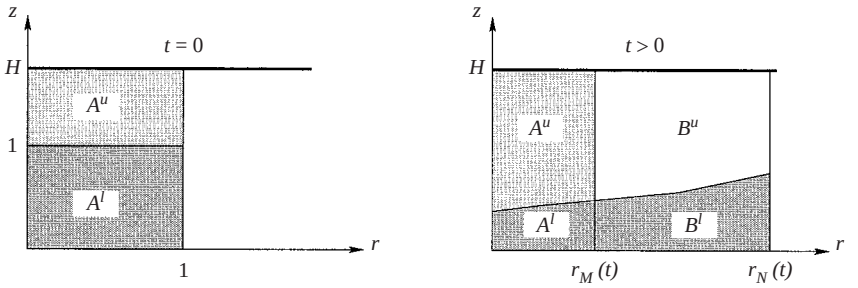

FIGURE 4. Sketch of upper regions A^u (ambient fluid initially above the dense fluid in the lock) and B^u (added ambient fluid to layer 2 during propagation of the current) and the lower regions A^l and B^l of dense fluid. At the initial time the region B does not exist.

nose at time t has not been displaced from its initial radial position, and consequently maintains its initial zero angular velocity.

(v) The necessary boundary conditions for h_1 at $r = 0$ and r_N are provided implicitly by the characteristics discussed in Appendix A. This means that the SW formulation is well-posed only when the characteristics from inside the dense fluid domain propagate smoothly to these positions, and restrictions on the straightforward solution emerge. First, at $t = 0^+$ the height of the nose must be assumed to drop instantaneously from $h_N = 1$ to a smaller value (typically 0.4, depending on the Fr correlation) for which the characteristic velocity matches that of the nose and, secondly, the initial height ratio H in the two-layer model must be larger than 2, as pointed out by Rottman & Simpson (1983). The latter restriction can apparently be relaxed by a special treatment of the region $r < 1$ during the initial period of propagation, see Klemp *et al.* (1994) and Zemach (2002), but this refinement was beyond the objectives of the present study.

(vi) The position of the nose as a function of time is given by the kinematic condition

$$\frac{\mathrm{d}}{\mathrm{d}t} r_N(t) = u_1(r_N, t). \tag{4.18}$$

4.3. *The connection between the angular velocities of the lower and upper layers*

It is well-known that, in the two-layer SW formulation, the average radial velocities in the upper and lower layers are connected by the simple algebraic formula (4.9), a straightforward consequence of volume conservation. We show here that, in the considered configuration, the average angular velocities in the upper and lower layers are also connected by some beneficial algebraic formulae. This is a consequence of more complex conservation balances, as follows.

First, we note that the potential vorticity is conserved under the assumptions of the present SW model in both layers, $i = 1, 2$. This result, in dimensionless form, can be expressed as

$$\frac{\mathrm{D}}{\mathrm{D}t}\left(\frac{\zeta_i + 2}{h_i}\right) = 0, \tag{4.19}$$

where

$$\zeta_i = \frac{1}{r}\frac{\partial}{\partial r}(r^2\omega_i) \tag{4.20}$$

is the axial vorticity component (scaled with Ω) (e.g. see Dewar & Killworth 1990; Ungarish & Huppert 1998).

The initial condition is simply

$$\zeta_1 = \zeta_2 = 0 \quad (t = 0). \tag{4.21}$$

However, the implementation of the foregoing potential vorticity balances is complicated by the fact that the fluid in the domain of interest ($0 \leqslant r \leqslant r_N,\ 0 \leqslant z \leqslant H$) is composed of bulks which carry different values of potential velocity, because of their different initial positions in the process. To sort this out, we split the domain into four regions, A and B each with an upper and lower part, see figure 4.

Region A^u : $h_1 \leqslant z \leqslant H$; $0 \leqslant r \leqslant r_M(t)$
contains the volume of ambient fluid which at $t = 0$ was located above the 'locked' dense fluid. The volume is $\pi(H-1)$ and $r_M(0) = 1$.
Region B^u : $h_1 \leqslant z \leqslant H$; $r_M(t) \leqslant r \leqslant r_N(t)$
contains the volume of ambient fluid which entered the upper layer after the release of the current.
Region A^l : $0 \leqslant z \leqslant h_1$; $0 \leqslant r \leqslant r_M(t)$
contains the dense fluid below the ambient fluid of region A^u.
Region B^l : $0 \leqslant z \leqslant h_1$; $0 \leqslant r_M(t) \leqslant r_N(t)$
contains the dense fluid below the ambient fluid of region B^u.

Here, $r_M(t)$ denotes the radius of the region A, which is provided implicitly by the volume conservation

$$2\pi \int_0^{r_M(t)} (H - h_1(r,t)) r \, \mathrm{d}r = \pi(H-1); \tag{4.22}$$

evidently, $(1 - H^{-1})^{1/2} < r_M < 1$ (for $0 < h_1 < 1$).

Consider $0 \leqslant r < r_M(t)$. Initially, the fluid particles located in the upper region A^u are of height $h_2 = H - 1$, and those in the region A^l below are of height $h_1 = 1$.

We start with the upper region A^u. Equations (4.19) and (4.21) combine into

$$\frac{\zeta_2 + 2}{H - h_1} = \frac{2}{H-1}, \tag{4.23}$$

and provide, recalling the relationship (4.20) between ζ and ω,

$$h_1(r,t) = 1 - \tfrac{1}{2}(H-1)\frac{1}{r}\frac{\partial}{\partial r}(r^2\omega_2). \tag{4.24}$$

Substitution of (4.24) into (4.22) yields

$$2\pi(H-1)\left[\tfrac{1}{2}r_M^2 + \tfrac{1}{2}r_M^2\omega_2(r_M)\right] = \pi r_M^2(H-1), \tag{4.25}$$

which can be rewritten as

$$\omega_2(r_M-, t) = -1 + \left[\frac{1}{r_M(t)}\right]^2, \tag{4.26}$$

which actually expresses angular momentum conservation for a ring of fluid which moved from $r = 1$ inwardly to r_M. (We used r_M- because at this stage it is not known whether ω_2 is continuous at the border between regions A and B.)

In the lower region A^l, the potential vorticity conservation reads

$$\frac{\zeta_1 + 2}{h_1} = 2. \tag{4.27}$$

We eliminate h_1 from (4.27) and (4.23) to obtain:

$$\frac{\partial}{\partial r}(r^2\omega_1) = -(H-1)\frac{\partial}{\partial r}(r^2\omega_2). \tag{4.28}$$

Integration of (4.28), subject to the condition of regularity of the angular velocity at $r = 0$, provides the following connection between the lower-layer and upper-layer angular velocity

$$\omega_2(r) = -\frac{1}{H-1}\omega_1(r) \qquad (0 \leqslant r < r_M(t)). \tag{4.29}$$

Consider $r_M(t) < r \leqslant r_N(t)$. Initially, the fluid particles located in the upper region B^u are of height $h_2 = H$, and those in the region B^l below are of height $h_1 = 1$. Consequently, (4.27) holds in B^l, while in B^u the corresponding balance is

$$\frac{\zeta_2 + 2}{H - h_1} = \frac{2}{H}. \tag{4.30}$$

We eliminate h_1 from (4.27) and (4.30) to obtain:

$$1 + \frac{1}{2}\frac{1}{r}\frac{\partial}{\partial r}(r^2\omega_1) = -\tfrac{1}{2}H\frac{1}{r}\frac{\partial}{\partial r}(r^2\omega_2). \tag{4.31}$$

Integration of the last equation subject to the boundary conditions (4.16) and (4.17) gives the following connection between the lower-layer and upper-layer angular velocity:

$$\omega_2(r) = -\frac{1}{H}\left[\omega_1(r) + 1 - \frac{1}{r^2}\right] \qquad (r_M(t) < r \leqslant r_N(t)). \tag{4.32}$$

Finally, consider the behaviour at the position $r = r_M(t)$. The angular velocity of the lower layer, ω_1, is continuous at this point because all the fluid in this layer emerged from behind the lock. With this observation in mind, we calculate $\omega_1(r_M)$ using (4.26) and (4.29), then substitute it into (4.32). The result is that ω_2 is also continuous at r_M.

We can therefore summarize the foregoing results into a compact analytical connection between the angular velocities in the upper and lower layers

$$\omega_2 = \begin{cases} -\dfrac{1}{H-1}\omega_1 & (0 \leqslant r \leqslant r_M), \\ -\dfrac{1}{H}\left[\omega_1 + 1 - \dfrac{1}{r^2}\right] & (r_M \leqslant r \leqslant r_N), \end{cases} \tag{4.33}$$

where $r_M(t)$ is defined by (4.22).

Evidently, for $H \to \infty$, the one-layer assumption $\omega_2 = 0$ is recovered. On the other hand, when $H \to 1$, we expect $\omega_2 \to \infty$ for $r \leqslant r_M$. This non-physical result indicates that viscous terms cannot be neglected in this case in the (actually very small) domain where ω_2 is large.

An important implication of (4.33) is the possibility of discarding one of the two partial differential equations for the azimuthal (angular) velocities in the system which governs the average motion in the two-layer system, and calculate the discarded variable (say, ω_2) from (4.33). A similar possibility has been developed for the radial velocity by Rottman & Simpson (1983), as already mentioned. The conclusion is that, after the foregoing manipulations of the two-layer model, it is necessary to solve the governing equations only for one layer (say, the lower one, with subscript 1).

The directly obtained variables (h_1, u_1, ω_1) provide the corresponding upper-layer counterparts via the simple algebraic connections (4.8)–(4.9) and (4.33).

We observe that the inviscid SW approximation predicts a discontinuity of angular velocity between the dense and ambient fluid both at the nose ($r = r_N$) and along the interface ($z = h$), but the angular velocity of the ambient remains continuous during the propagation.

Finally, we note the connection between the angular velocity boundary condition (4.16) and the potential vorticity conservation (4.19) for $i = 1$. If we formulate the volume conservation in the lower layer, with h_1 defined via (4.27) and ζ_1 replaced by (4.20), we recover (4.16).

4.4. *Integration of the time-dependent SW equations*

The SW time-dependent system of hyperbolic PDEs and appropriate boundary conditions must be solved by numerical methods. Although we are able to reduce the two-layer model to a set of partial differential equations for the variables of one layer only, a fundamental difference remains between the one- and two-layer models. In the genuine one-layer model, the characteristics cover smoothly the entire domain of the dense fluid, but in the two-layer model some non-physical behaviour of characteristics may appear for values of H smaller than about 2. Actually, the two-layer model predicts that for $H < 2$, shortly after the release, the backward-moving depression wave of the interface develops into a steep 'jump'. This backward-moving shock wave needs special consideration, as discussed by Rottman & Simpson (1983), Klemp, Rotunno & Skamarock (1994) and Zemach (2002), but complete remedies have been suggested only for rectangular geometries. In order to avoid these complications, we restrict our two-layer solutions to $H > 2.3$. This topic will be reconsidered in the next section. The SW system of hyperbolic equations is essentially amenable to solution by the method of characteristics, as used by Rottman & Simpson (1983) for the rectangular case. However, here we are concerned with the complicated extension to a cylindrical coordinate system and the incorporation of angular momentum balances, and the use of a fixed (prescribed) numerical grid is advantageous. We therefore use the finite-difference discretization of the original equations by a two-step Lax–Wendroff method (see Anderson *et al.* 1984; Press *et al.* 1992), which produces, as shown below, a convenient efficient and flexible numerical code.

To facilitate the implementation of the boundary conditions, the time-dependent physical r-domain of interest was mapped into a time-independent computational domain by

$$y = \frac{r}{r_N(t)} \qquad (0 \leqslant y \leqslant 1). \tag{4.34}$$

Consequently, the SW equations were subjected to the following coordinate transformations:

$$\left(\frac{\partial}{\partial t}\right)_r = \left(\frac{\partial}{\partial t}\right)_y - y\frac{\dot{r}_N}{r_N}\left(\frac{\partial}{\partial y}\right)_t, \qquad \left(\frac{\partial}{\partial r}\right)_t = \frac{1}{r_N}\left(\frac{\partial}{\partial y}\right)_t, \tag{4.35}$$

where the over dot denotes time derivative. Following the approach of Bonnecaze, Huppert & Lister (1993) and Ungarish & Huppert (1998), we performed the numerical solution using a finite-difference two-step Lax–Wendroff method. For efficient implementation of this scheme, the governing equations (4.2), (4.10) and (4.6), supplemented by (4.8)–(4.9) and (4.33), are formulated in conservation form for

the variables $h = h_1$, $q = u_1 h_1$ and $s = v_1 h_1$

$$\begin{cases} \dfrac{\partial h}{\partial t} = \dfrac{1}{r_N}\left[y\dot{r}_N \dfrac{\partial h}{\partial y} - \dfrac{\partial q}{\partial y}\right] - \dfrac{q}{r}, \\ \dfrac{\partial q}{\partial t} = \dfrac{1}{r_N}\left[\left(y\dot{r}_N - \dfrac{B}{A}\dfrac{q}{h} - \dfrac{q}{h}\right)\dfrac{\partial q}{\partial y} + \left(\dfrac{B}{A}\dfrac{q^2}{h^2} - \dfrac{C}{A}h\right)\dfrac{\partial h}{\partial y}\right] + h\dfrac{D+E}{A} - \dfrac{q^2}{hr_N y}, \\ \dfrac{\partial s}{\partial t} = \dfrac{1}{r_N}\left[y\dot{r}_N \dfrac{\partial s}{\partial y} - \dfrac{\partial}{\partial y}\left(\dfrac{qs}{h}\right)\right] - 2q\left[1 + \dfrac{s}{hr_N y}\right]. \end{cases} \tag{4.36}$$

Smoothing of spurious oscillations was achieved by use of a small artificial viscosity term added to the radial momentum equation. The obvious boundary conditions are (4.13)–(4.18). In addition, boundary conditions for h (at $y = 0, 1$) are necessary, and calculated for each new time step from the balances on the characteristics λ_-, λ_+, see the Appendix. Note that the velocity $\mathrm{d}y/\mathrm{d}t$ is obtained by the transformation $[\mathrm{d}r/\mathrm{d}t - y\dot{r}_N]/r_N$ of the characteristic velocities in the physical domain.

After obtaining the variables in the lower layer, the counterparts in the upper layer are readily calculated with the aid of (4.8)–(4.9) and (4.33). A typical computation using a grid of 100 intervals can be performed in about 1 min on a common workstation. Results will be presented in § 5.

4.5. *Steady-state lens (SL)*

The SW equations admit a steady-state solution with $u = 0$ and $r_N = \text{const}$. Letting $y = r/r_N$, the governing system is given by the radial momentum and potential vorticity equations, (4.10) and (4.27), for $0 \leqslant y \leqslant 1$, as follows

$$\frac{\mathrm{d}h_1}{\mathrm{d}y} = \mathscr{C}^2 r_N^2 y[\omega_1(2+\omega_1) - \omega_2(2+\omega_2)], \tag{4.37}$$

$$h_1 = 1 + \omega_1 + \tfrac{1}{2} y \frac{\mathrm{d}\omega_1}{\mathrm{d}y}, \tag{4.38}$$

subject to the relationship (4.33), the boundary conditions (4.13), (4.16) and $h(y = 1) = 0$. Substitution of (4.38) and (4.33) into (4.37) yields a single equation for ω_1. The solution provides r_N of the lens, $\omega_1(y)$ and $h(y)$. An equivalent system was formulated by Dewar & Killworth (1990). In general, the solution is performed by numerical methods, with some iterations on the nonlinear right-hand side of (4.37) and value of r_N. We used a finite-difference discretization on a 50 interval grid, and performed iterations for obtaining the proper nonlinear combination of $\omega_1(y)$ and r_N. The initial 'guess' was $\omega_1(y) = \omega_1(1)$ and $r_N = 1.05(2/\mathscr{C})^{1/2}$; then, a new value of r_N was deduced by imposing the $h(1) = 0$ boundary condition, and so on. Usually, after about nine iterations, convergence to at least five significant digits was achieved.

In the one-layer case, the solution is simplified by the fact that $\omega_2 = 0$, and analytical approximations can be obtained. Assume an expansion in powers of $\mathscr{C}$ (for small values of this parameter) as follows

$$\omega_1 = -1 + \mathscr{C}\left(o_{(1)} + \mathscr{C}^2 o_{(2)} + \mathscr{C}^4 o_{(3)} + \dots\right), \tag{4.39}$$

$$r_N^2 = \frac{1}{\mathscr{C}}\left[R_{(1)} + \mathscr{C}^2 R_{(2)} + \mathscr{C}^4 R_{(3)} + \dots\right]. \tag{4.40}$$

Substitution in the equation for ω_1 and the related boundary conditions and solving separately for increasing powers of $\mathscr{C}$ we obtain

$$o_{(1)} = 1 - \tfrac{1}{2}y^2, \tag{4.41}$$

$$o_{(2)} = \frac{-17 + \frac{37}{2}y^2 - 8\,y^4 + y^6}{48}, \tag{4.42}$$

$$o_{(3)} = \frac{3731}{23\,040} - \frac{y^2\left(10075 - 6880\,y^2 + 2540\,y^4 - 480\,y^6 + 32\,y^8\right)}{46\,080}. \tag{4.43}$$

and

$$R_{(1)} = 2; \quad R_{(2)} = \tfrac{11}{24}; \quad R_{(3)} = -\tfrac{193}{2304}. \tag{4.44}$$

The corresponding approximation for $h(y)$ follows from the substitution of (4.39) into (4.38),

$$h_1 = \mathscr{C}\left[o_{(1)} + \tfrac{1}{2}yo'_{(1)} + \mathscr{C}^2\left(o_{(2)} + \tfrac{1}{2}yo'_{(2)}\right) + \mathscr{C}^4\ldots\right] = \mathscr{C}[1 - y^2 + \mathscr{C}^2\ldots]. \tag{4.45}$$

We note that Nof & Simon (1987) and Ungarish & Huppert (1998) presented identical results for the leading terms with subscript (1) in this expansion, but did not derive the next terms.

The accuracy of this three-term expansion was verified via a comparison to the numerical solution. For h_1 and ω_1, the maximal error is at the centre and decays with y. For $\mathscr{C}^2 = 0.4$ (and smaller), the error is less than 0.5%, and even for $\mathscr{C} = 1$ the maximal error is only about 7%. The numerical value of r_N is larger than the asymptotical one, but the agreement is remarkably good: the discrepancy is only 0.6% for $\mathscr{C} = 1$.

We could not find simple analytical approximations for the SL in the two-layer formulation. However, the influence of the upper layer on the behaviour of the SL can be easily inferred from a numerical example. We considered the results for values of $\mathscr{C} = 0.2$ and 0.4 and various H. We found that the presence of the upper layer hinders the expansion of the lens, but the effect on r_N is small. For $H = 10$, the values of r_N are very close to the one-layer results (3.18 and 2.27 for $\mathscr{C} = 0.2$ and 0.4), and when H changes from 10 to 1.05, r_N is reduced by 6% for $\mathscr{C} = 0.4$, and 4% for $\mathscr{C} = 0.2$. Additional details are displayed in figure 5. For the variables h_1, ω_1 and ω_2, the strongest influence is observed near the centre, mostly in the domain $r < r_M$. In this region, as H decreases, h_1 and ω_2 increase, the latter almost as $(H-1)^{-1}$; this effect is more pronounced for smaller $\mathscr{C}$. However, for $r > r_M$, the function ω_2 decays with r and the influence of the upper layer is weak. The position r_M is easily identified in figure 5(*c*) as the radius of maximum ω_2.

The shape of h_1 is in agreement with the results of Dewar & Killworth (1990). In particular, Dewar & Killworth (1990) pointed out that, for $H \to 1$, the lens tends to maintain a 'point of surface contact', i.e. $h_1(r = 0) \to 1$, in strong contrast with the value $h_1(r = 0) = \mathscr{C}$ expected for a deep lens ($H \gg 1$). This is confirmed in figure 6, which displays h_1 as a function of r^* scaled with the Rossby radius of deformation, $r_0/\mathscr{C}$, and therefore our results for H close to 1 can be straightforwardly compared with small δ cases in figure 4 of that paper. However, the initial depth ratio H influences the shape of the lens near the centre only, where a small volume of the dense fluid is present, even for the extreme $H \approx 1$ case. We also observe that the radius of the lens is significantly larger than the Rossby radius of deformation in the presented case with a small value of $\mathscr{C}$. The stability of the SL, mostly for

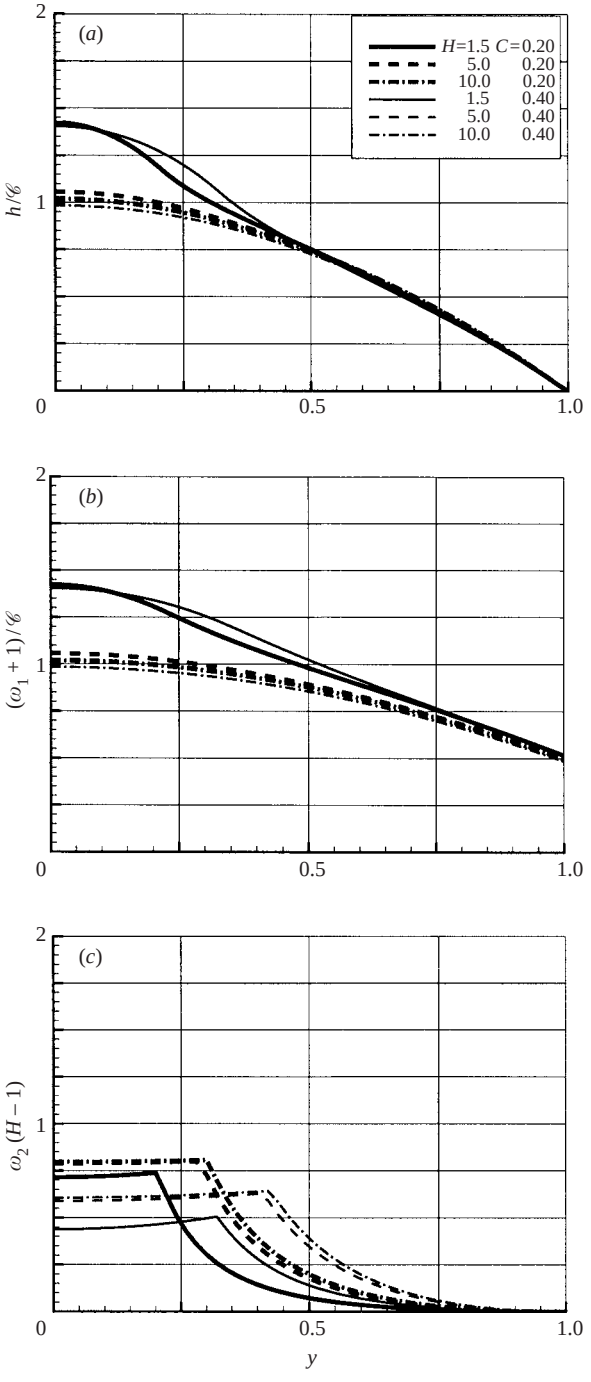

FIGURE 5. Two-layer steady lens results for various H, $\mathscr{C} = 0.2$ and 0.4: (*a*) $h/\mathscr{C}$, (*b*) $(\omega_1 + 1)/\mathscr{C}$ and (*c*) $\omega_2\ (H - 1)$ as functions of y.

non-small values of $\mathscr{C}$ has been considered both experimentally and theoretically (see Griffiths & Linden 1981; Holford 1994; Choboter & Swaters 2000 and the references therein), but this topic is beyond the scope of the present work.

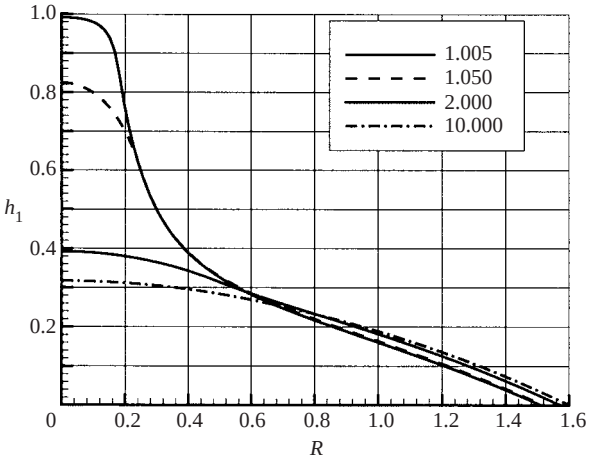

FIGURE 6. Two-layer steady lens results for various H, $\mathscr{C}^2 = 0.1$: h_1 as a function of radius scaled with the Rossby radius of deformation, $r_0/\mathscr{C}$.

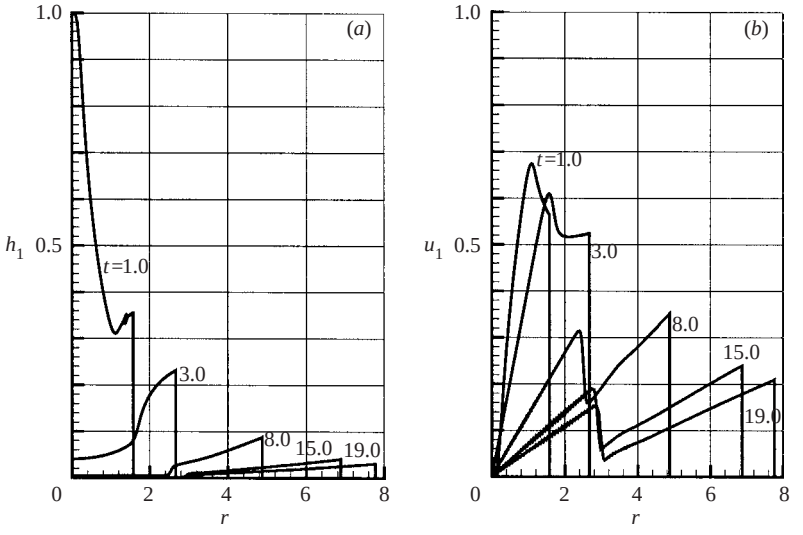

FIGURE 7. SW two-layer results for a *non-rotating* axisymmetric current with $H = 2.4$: (*a*) interface h_1 *vs.* r, various t; (*b*) radial velocity u_1 *vs.* r, various t.

5. Results of SW and NS calculations

Typical results of the shallow-water approximation in various axisymmetric configurations without and with rotation are presented in figures 7–9. (The calculations were performed on a grid of 200 points with a time step of 10^{-3}, and confirmed by convergence tests on both finer and coarser grids.)

Figure 7, for a non-rotating current, shows the behaviour of the interface, h_1, and radial velocity, u_1, in the dense fluid (current) domain. The 'nose-up' shape and positive u during the entire period of propagation are typical of the non-rotating configuration. We also note that a 'throat' depression of the interface appears around $r = 1$ in the initial times of propagation of the axisymmetric current (figure 7*a*, the $t = 1$ line), unlike the constant h_1 portion that trails the nose in the rectangular

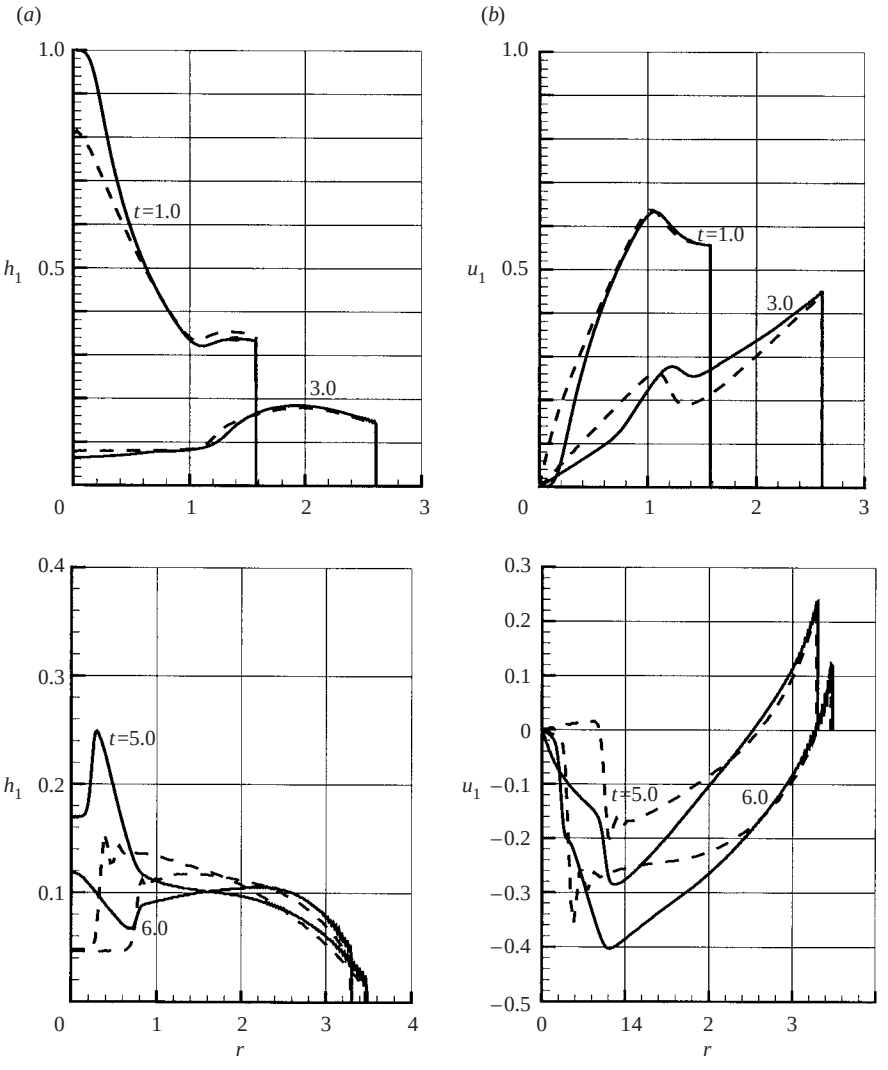

FIGURE 8. SW one-layer —, and - - -, two-layer results for a rotating axisymmetric current with $\mathscr{C} = 0.3$ and $H = 2.4$: (*a*) interface h_1 *vs.* r, various t; (*b*) radial velocity u_1 *vs.* r, various t.

current during the initial 'slumping' phase. This is a result of the curvature terms, and is later reflected in the interesting double-peaked structure of the u_1 profiles (figure 7*b*). However, the first peak occurs in a very thin layer of fluid where viscous effects may become dominant, and hence a clear-cut experimental verification of this behaviour may be a difficult task.

The corresponding results of the shallow-water equations in a rotating frame with $\mathscr{C} = 0.3$ are presented in figure 8. The one- and two-layer results are in good qualitative and quantitative agreement, and display the same differences to the non-rotating case. The two-layer model predicts a slightly faster propagation. At the beginning of the motion ($t \leqslant 1$), the rotating current behaves like the non-rotating counterpart. At $t \approx 3$ ($\mathscr{C}t \approx 0.9$, about one-tenth of a revolution of the system), the leading part of the rotating current displays a 'nose-down' shape, which reflects the hindering Coriolis

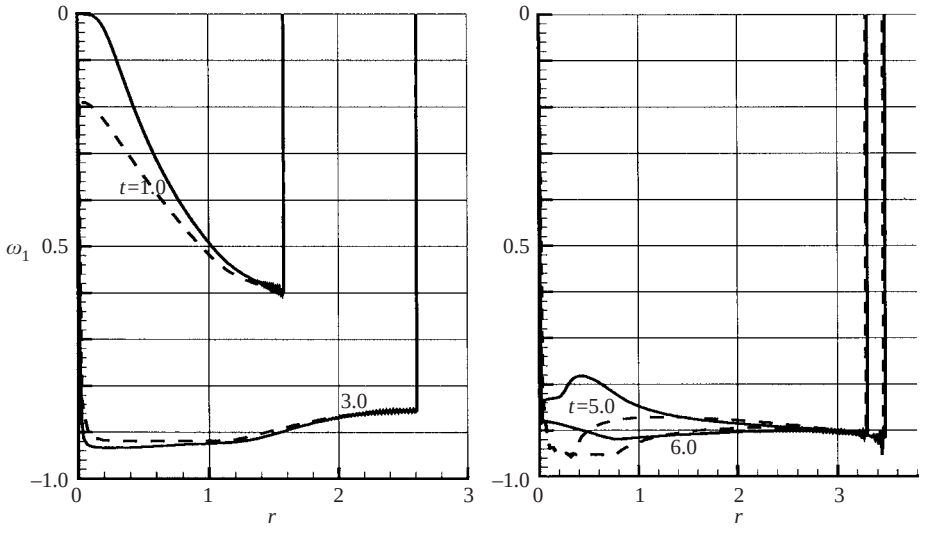

FIGURE 9. SW one-layer —, and - - -, two-layer results for rotating axisymmetric current with $\mathscr{C} = 0.3$ and $H = 2.4$: angular velocity ω_1 *vs.* r, various t.

effects. At $t = 5$, a significant reverse radial motion is present in the rotating current, and at $t = 6$ ($\mathscr{C}t = 1.8$, about one-third of a revolution of the system), the height and velocity of the nose are close to zero. The maximal radius of propagation is ≈ 3.5, about 35% larger than that of the steady lens, cf. (4.40) and (4.44). This indicates an energy excess that must be dissipated and the possibility of contraction–expansion oscillations. However, the present SW model is not expected to be valid for this stage, and, in particular, viscosity and wave-breaking effects are bound to change the nose condition (4.14), see (Killworth 1992). This topic is not pursued here.

The angular velocity of the propagating dense fluid is displayed in figure 9. We observe that ω_1 is negative and quickly (at $\mathscr{C}t \approx 0.6$, say) attains a value close to -1 in the entire dense-fluid domain. This means that the angular motion of the current lags considerably behind that of the ambient current. The one- and two-layer model predictions are, again, in good agreement, in particular in the region $r > 1$.

The oscillations with r observed in the SW results are attributed to spurious numerical modes. It was verified that they could be smoothed by an increased artificial viscosity, but this increase of dissipation may also affect the speed of propagation of the current.

A major conclusion, based on this example and other similar results with various values of $\mathscr{C}$ and H, is the very good agreement between the one-layer and two-layer model predictions for the motion of a rotating gravity current. The difference appears mostly near the centre, and hence affects only a small portion of the volume of the moving fluid. The interpretation of this observation is as follows.

Consider the SW equations of motion and recall that we reduced them to the solution of the lower layer only. The influence of the rotation (represented by the parameter $\mathscr{C}$) on the radial propagation enters only via the Coriolis-centrifugal term E on the right-hand side of the radial momentum equation (4.10). This term can be rewritten as

$$-\mathscr{C}^2 r[-\omega_1(2+\omega_1) + \omega_2(2+\omega_2)]. \tag{5.1}$$

Run	Geometry	H	h_0/r_0	r_w	$\mathscr{C}$	$il \times jl$
1-2D	Rectangular	1.25	0.36	5	0	250×100
2-2D	Rectangular	2.50	0.36	5	0	250×100
1-R	Axisymmetrical	1.25	0.36	4	0.3	160×150
1a-R	Axisymmetrical	1.25	0.36	4	0.3	320×210
2-R	Axisymmetrical	2.50	0.36	4	0.3	200×150
1-NR	Axisymmetrical	1.25	0.36	4	0	160×150
2-NR	Axisymmetrical	2.50	0.36	4	0	200×150

TABLE 1. NS runs data. In all cases: $\epsilon = 10^{-3}$, $Re = 6 \times 10^4$.

Quickly, after the propagation of about one radius, $\omega_1 \approx -1$ and the first term in the square brackets becomes very close to 1. The second term in these brackets is positive, and its magnitude (compared to unity) determines the influence of the additional Coriolis terms in the upper layer. We use (4.33) to obtain the estimate $\omega_2 \approx 1/Hr^2$ for $r > 1 > r_M$. Thus, the relative contribution of the upper layer to the Coriolis term for large r is about $2/Hr^2$, and typically very small, because the radius of propagation is about $(2/\mathscr{C})^{1/2}$. The relative contribution of the upper layer to the Coriolis term may be large for small r, but this domain has little significance to the global motion of the current. The physical interpretation of the foregoing estimates is that the angular velocity in the upper layer produces only a small perturbation of the solid-body-rotation pressure field in the ambient fluid.

Navier–Stokes (NS) simulations were performed for several configurations as detailed in table 1. The accuracy of the numerical results was confirmed by testing different time steps and grids (in particular in the runs of rotating cases 1-R and 1a-R). The computations on the fine grid, 320 horizontal and 200 vertical intervals, require considerable amounts of both CPU time (to advance the flow field by a dimensionless time interval of 1 it took about 11 CPU hours on an SG Origin computer with R10000/3.4 250 MHz processors) and storage space. This is in strong contrast with the SW solutions which require only several CPU seconds for the corresponding task.

Figure 10 displays results for two rectangular (non-rotating) currents, of initial depth ratios $H = 1.25$ and 2.5, at times $t = 1$ and 2. This figure shows that the shape of the current is (i) little affected by the value of H, and (ii) significantly different from the predictions of the SW model. In particular, we recall that for $H < 2$, the SW two-layer model predicts that the interface contains a steep backward-moving portion (jump) during the initial collapse (say, $t < 2$). In the NS results, no such jump is observed in both the density and velocity fields. On the other hand, as shown in figure 11, the distance of propagation as a function of time predicted by the NS simulations is in good agreement with the SW results of both the one- and two-layer models. We note in passing that the velocity of propagation predicted in the present case by the SW models (in particular the two-layer one) is also in good agreement with experimental data (Ungarish & Zemach 2003).

Figure 12 displays corresponding results for the axisymmetric (non-rotating) current at times $t = 1$ and 2 for the initial depth ratios $H = 1.25$ and 2.5. As in the rectangular case, the shape of the current is (i) little affected by the value of H, and (ii) significantly different from the prediction of the SW model. The nose of the axisymmetric current is lower and the speed of propagation decreases faster than in the case of the rectangular current with similar initial release conditions; this is a consequence of the

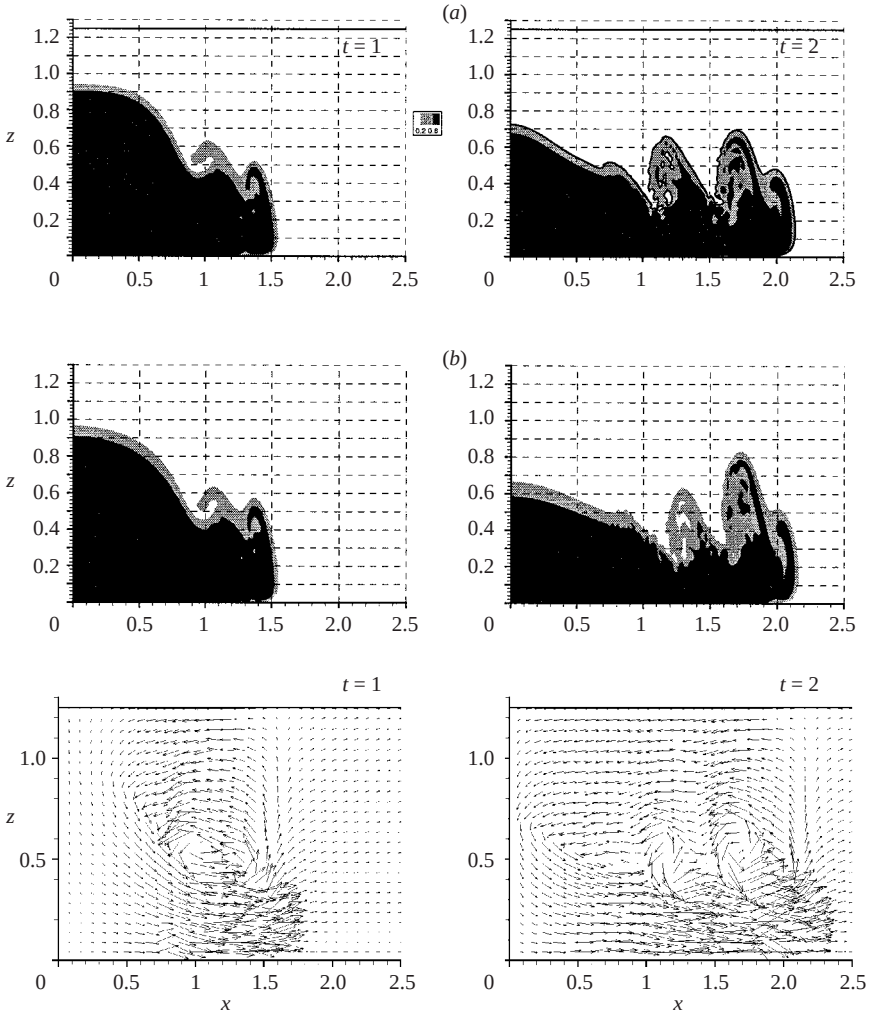

FIGURE 10. Rectangular gravity currents, NS results. Density function contours for (*a*) $H = 1.25$ and (*b*) $H = 2.50$ at $t = 1$ and 2; also shown the velocity vector plot for $H = 1.25$.

curvature effect on the volume continuity. This behaviour is consistent with the SW predictions. Again, good agreement between the NS and SW results of the distance of propagation as a function of time was obtained for these times, see figure 14. Some recent experiments indicate good agreement of r_N *vs.* t with SW model predictions (figure 4 in Hallworth *et al.* 2001).

The NS predicted behaviour of a rotating current with $\mathscr{C} = 0.3$ and $H = 1.25$ is illustrated in figures 13–15. The computation was performed on a relatively fine grid, with 320 radial and 210 stretched intervals, and a time step of 2×10^{-4}. We note that very close results were obtained also on a coarser grid (160×150 intervals).

The density contours in figure 13 show the complex shape of the interface, with regions of mixing and entrainment. The Coriolis effects cause, at $t = 4$ and 6, an evident reverse flow manifested by accumulation of fluid in the centre. At $t = 6$, the outer ring of dense fluid seems to separate from the main bulk of the current at $r \approx 2.5$.

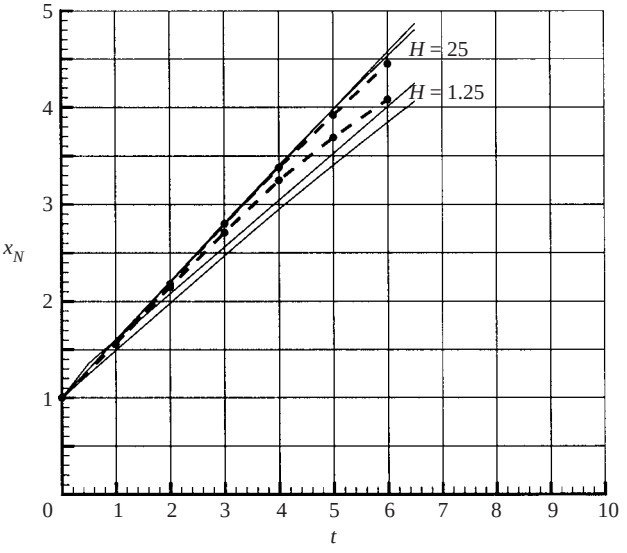

FIGURE 11. Length of propagation as function of time of rectangular currents with $H = 1.25$ and 2.5, as predicted by –– ●, NS and —, SW one- and two-layer models (the slightly higher line is for the two-layer model).

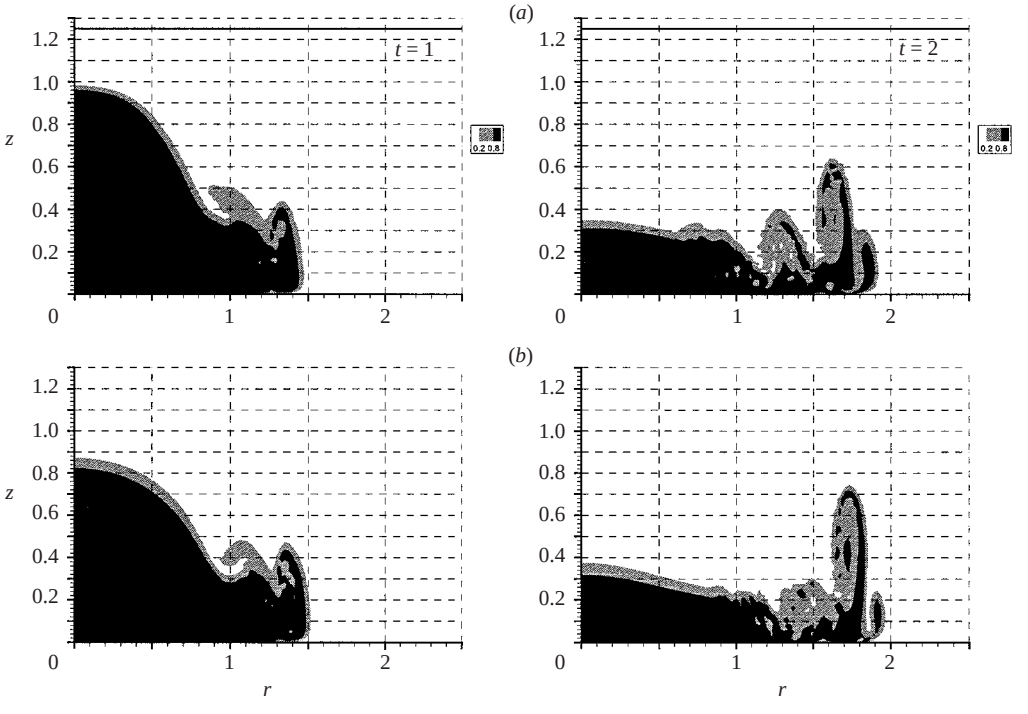

FIGURE 12. Axisymmetric non-rotating gravity currents, NS results. Density function contours for (*a*) $H = 1.25$ and (*b*) $H = 2.50$ at $t = 1$ and 2.

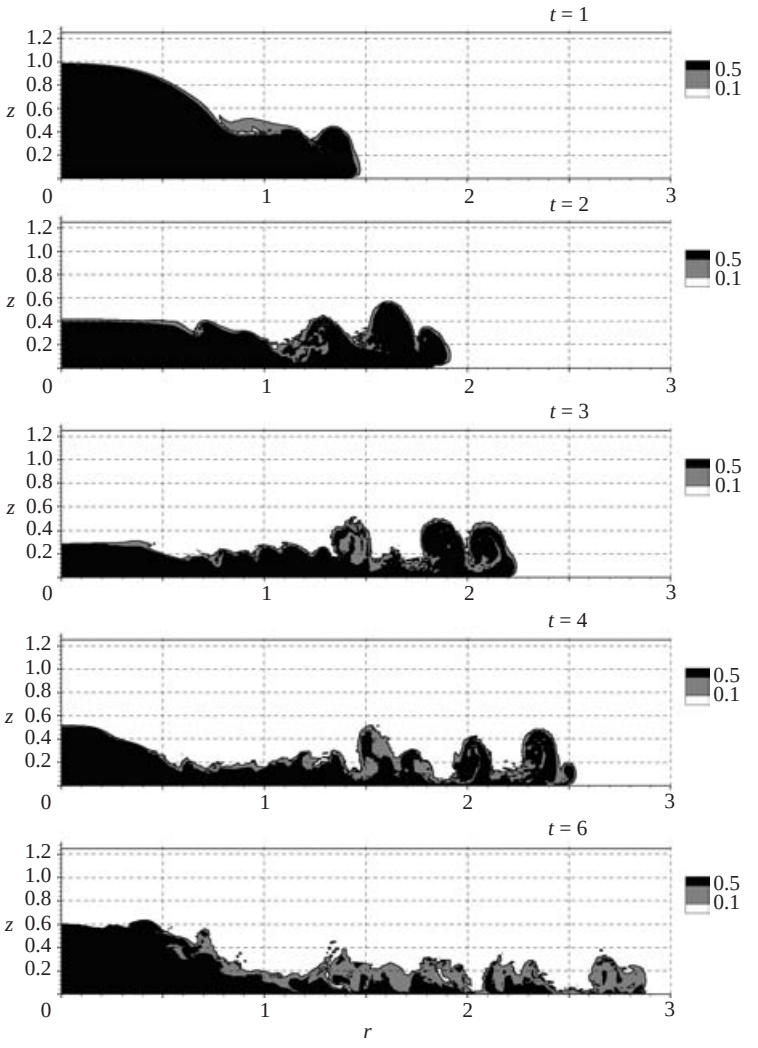

FIGURE 13. Rotating current with $\mathscr{C} = 0.3$ and $H = 1.25$, density contours at various times predicted by NS (320×210 grid).

The time-dependent behaviour of the radius of propagation of the rotating current is shown in figure 14. We display the NS predictions for both the rotating and the non-rotating currents (circle and square symbols, respectively) and the corresponding SW approximations with a one-layer model (solid lines). All results practically coincide for $t \leqslant 2$. Afterwards, the NS propagation is slightly slower than the SW prediction, which we attribute to the mixing/entrainment effects. In addition, for $t > 2$, the Coriolis effects hinder the propagation of the rotating current, as clearly seen in both NS and SW results. The SW predicts that the maximal radius is attained at $t \approx 6$ (0.3 revolutions). A close inspection of the NS results indicates that at this time the head region of the current is not sharply defined: the dense fluid in the ring $2.4 < r < 2.8$ is quite diluted and apparently detached from the main body of the current. This uncertainty is indicated by the two NS points at $t = 6$ in figure 14. Overall, there is fair agreement between SW and NS predictions concerning the distance of propagation.

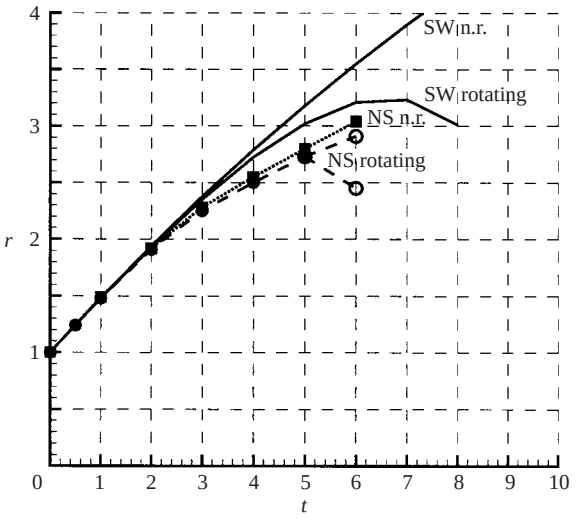

FIGURE 14. Radius of propagation as function of time, —, SW and ···, ---, NS predictions for currents with $H = 1.25$ non-rotating (n.r.) and rotating with $\mathscr{C} = 0.3$. The two points of the rotating current at $t = 6$ indicate the spread of the head.

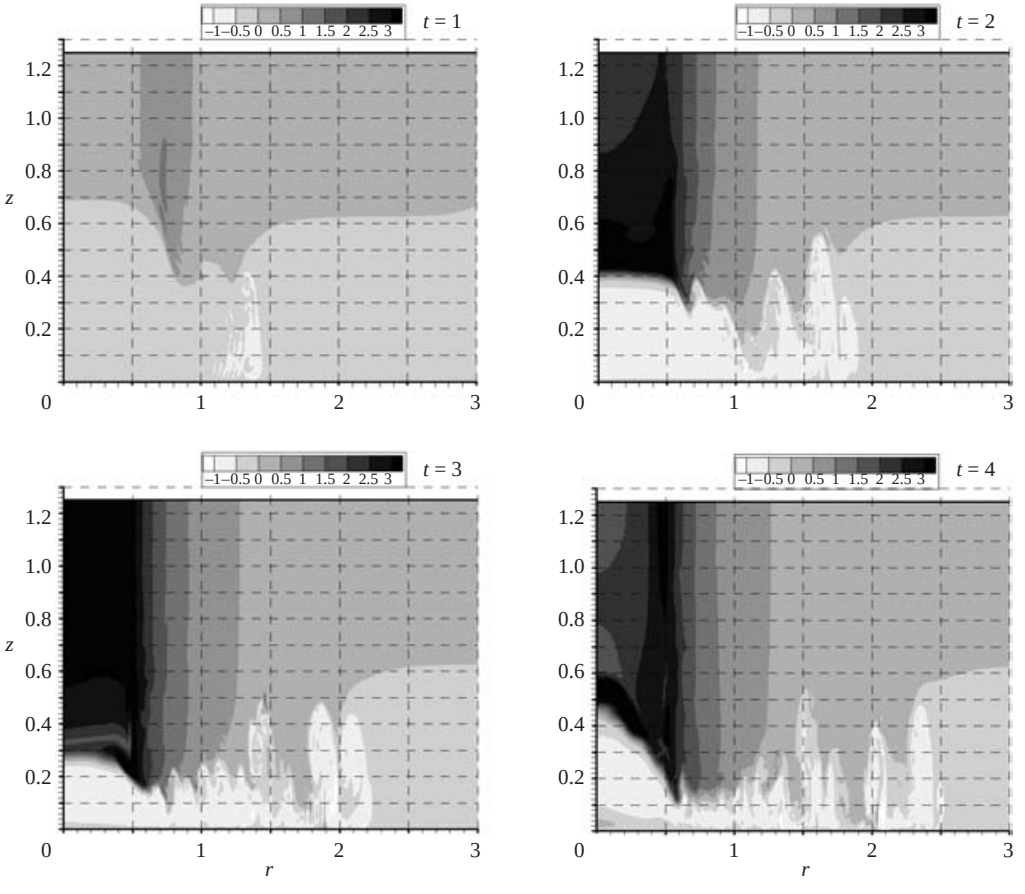

FIGURE 15. Rotating current with $\mathscr{C} = 0.3$ and $H = 1.25$, angular velocity contours at various times predicted by NS (320×210 grid).

The above mentioned fade-out of the head of the rotating gravity current has been, qualitatively, observed in the laboratory experiments reported in Hallworth *et al.* (2001). It may explain the fact that for small values of $\mathscr{C}$, the NS calculations do not converge to the analytical steady-lens results. Killworth (1992) noted that a wave-breaking mechanism may be needed to accommodate the energy differences between the initial and final state of a 'collapsed cylinder' lens. Such an over-expanded lens is expected to contract and then oscillate, perhaps like the 'pulsons' studied by Rubino, Hessner & Brandt (2002) (where other references are given). However, the details of these effects require fine resolutions, beyond the accuracy of the present grids (and very likely also the inclusion of some non-axisymmetric modes). This topic is left for future investigations.

The angular velocity field is illustrated in figure 15. We notice that the current has a distinct 'signature', i.e. the angular velocity of the dense fluid is in clear contrast with that of the ambient. Moreover, we observe that after a short time, ω in the current is close to -1, while in the central region of the ambient fluid ($r < 0.5$, say) a large positive value of ω develops. In other words, while the current fluid loses its rotation relative to an inertial frame, the central core of the ambient fluid attains a swirl velocity about three times larger than the initial one. The positive swirl is, of course, a result of the inward radial motion of the fluid in the upper layer; in the corresponding configuration with $H = 2.5$ (not displayed) a much smaller swirl develops. Nevertheless, this strong swirl motion has little effect on the propagation of the current, because $r_N(t)$ is practically the same for both $H = 1.25$ and 2.5, see figure 14. Experimental measurement of the angular velocity field in a propagating gravity current is a difficult task and, to the best of our knowledge, these data have not been recorded. We hope that our results will motivate work in this direction.

6. Concluding remarks

We investigated the behaviour of axisymmetric gravity currents, released from behind a lock, in a rotating environment using shallow-water (SW) and finite-difference Navier–Stokes (NS) solutions. We focused attention on the case of small $\mathscr{C}$ (ratio of Coriolis to inertia terms) and large Re (ratio of inertia to viscous terms), but various H (height of ambient over initial height of the dense fluid).

We developed a two-layer SW formulation and obtained an explicit correlation between the angular velocities in the lower and upper layers. It was known that in the non-rotating case, the two-layer model can be reduced to the solution of two coupled PDEs for the dependent variables h and u of the dense layer only, and the corresponding variables in the upper layer are then obtained from explicit algebraic connections. Now we are able to extend this knowledge to the rotating current, with the addition of a PDE for the angular velocity ω in the dense layer whereas the corresponding variables in the upper layer are again obtained from simple algebraic connections. This procedure also simplifies the analysis and solution of the steady-state lens structures; however, a numerical solution is still necessary for the general two-layer lens problem, but an improved accurate asymptotical result was developed for the one-layer limit.

The two-layer SW current requires a 'nose' Froude-number condition which correlates the local velocity, u_N, to the local height of the dense fluid, h_N, taking into account the total height of the ambient, H. We found that the results of a one-layer model (i.e. with unperturbed ambient), subjected to the same Froude-number condition, are in very good agreement with the predictions of the two-layer model, except for a relatively small domain near the axis.

The full NS computations confirm the insights provided by the SW approximations, but also point out the very complex shape of the interface and the strong mixing/entrainment effect of a real current. The velocity of propagation of the characteristics of the SW model is not influenced by the rotation and hence difficulties of the type encountered in the rectangular (in particular two-layer) model may appear. The two-layer SW formulation becomes problematic when the initial height ratio H is smaller than 2; Rottman & Simpson (1983) pointed out the appearance of a backward-moving shock in the initial collapse phase, and Klemp *et al.* (1994), Zemach (2002) and Ungarish & Zemach (2003) show how to incorporate this singularity into the solution in a rectangular geometry. This complication has not been considered in the present work, but we argue that it is expected to be of little importance, because: (i) The NS results do not show any dramatic differences when H changes from 2.5 to 1.25 (and even closer to 1); we speculate that local viscous effects smooth out the 'jump' predicted by the inviscid theory. (ii) The modifications associated with this singularity are confined to a region close to the axis which, as already mentioned, has little influence on the propagation of the main body of the current. A detailed analysis of this topic is left for future work.

The assumption of axial symmetry is incompatible with some of the observed details concerning the motion and stability of real gravity currents. The investigation of the three-dimensional effects is a complex task and is also left for future work.

The research was partially supported by the Fund for the Promotion of Research at the Technion and by the Bar-Nir Bergreen Software Technology Center of Excellence.

Appendix. SW formulation in characteristic form

The characteristic form, paths and relationships are useful for the understanding of some features of the solution and for the application of the boundary conditions in the numerical solution of the SW equations.

The governing system (4.2), (4.10) and (4.6)–(4.7) can be rewritten as

$$\begin{pmatrix} h_{1t} \\ u_{1t} \\ v_{1t} \\ v_{2t} \end{pmatrix} + \begin{pmatrix} u_1\dfrac{\partial}{\partial r} & h_1\dfrac{\partial}{\partial r} & 0 & 0 \\ \dfrac{C}{A}\dfrac{\partial}{\partial r} & \dfrac{B}{A}u_1\dfrac{\partial}{\partial r} & 0 & 0 \\ 0 & 0 & u_1\dfrac{\partial}{\partial r} & 0 \\ 0 & 0 & 0 & -\dfrac{u_1h_1}{H-h_1}\dfrac{\partial}{\partial r} \end{pmatrix} \cdot \begin{pmatrix} h_1 \\ u_1 \\ v_1 \\ v_2 \end{pmatrix} = \begin{pmatrix} -\dfrac{u_1h_1}{r} \\ \dfrac{D+E}{A} \\ -u_1\left(2+\dfrac{v_1}{r}\right) \\ \dfrac{u_1h_1}{H-h_1}\left(2+\dfrac{v_2}{r}\right) \end{pmatrix}, \qquad (A\,1)$$

with corresponding eigenvalues of the matrix of coefficients which are:

$$\left.\begin{aligned}
\lambda_1 &= -\frac{u_1 h_1}{H - h_1}, \\
\lambda_2 &= u_1, \\
\lambda_+ &= \frac{u_1(A+B) + \left[u_1^2(A-B)^2 + 4CAh_1\right]^{1/2}}{2A}, \\
\lambda_- &= \frac{u_1(A+B) - \left[u_1^2(A-B)^2 + 4CAh_1\right]^{1/2}}{2A},
\end{aligned}\right\} \tag{A 2}$$

and the corresponding eigenvectors:

$$\left.\begin{aligned}
&(0, 0, 0, 1), \\
&(0, 0, 1, 0), \\
&\left(\frac{u_1(A-B) + \left[u_1^2(A-B)^2 + 4CAh_1\right]^{1/2}}{2Ah_1}, 1, 0, 0\right), \\
&\left(\frac{u_1(A-B) - \left[u_1^2(A-B)^2 + 4CAh_1\right]^{1/2}}{2Ah_1}, 1, 0, 0\right).
\end{aligned}\right\} \tag{A 3}$$

Consequently, the relationships between the variables on the characteristics with $\mathrm{d}r/\mathrm{d}t = \lambda$ are as follows:

$$\lambda_1 : \qquad \mathrm{d}v_2 = \frac{u_1 h_1}{H - h_1}\left(2 + \frac{v_2}{r}\right)\mathrm{d}t, \tag{A 4}$$

$$\lambda_2 : \qquad \mathrm{d}v_1 = -u_1\left(2 + \frac{v_1}{r}\right)\mathrm{d}t, \tag{A 5}$$

$$\lambda_+ : \qquad h_1\mathrm{d}u_1 + \left[\lambda_+ - u_1\frac{B}{A}\right]\mathrm{d}h_1 = h_1\frac{D+E}{A}\,\mathrm{d}t - \left[\lambda_+ - u_1\frac{B}{A}\right]\frac{u_1 h_1}{r}\,\mathrm{d}t, \tag{A 6}$$

$$\lambda_- : \qquad h_1\mathrm{d}u_1 + \left[\lambda_- - u_1\frac{B}{A}\right]\mathrm{d}h_1 = h_1\frac{D+E}{A}\,\mathrm{d}t - \left[\lambda_- - u_1\frac{B}{A}\right]\frac{u_1 h_1}{r}\,\mathrm{d}t. \tag{A 7}$$

Further manipulation yields a convenient boundary condition for v_1. Since on λ_2: $\mathrm{d}r/\mathrm{d}t = u_1$, (A 5) can be rewritten as:

$$\frac{\mathrm{d}v_1}{\mathrm{d}r} + \frac{v_1}{r} = -2. \tag{A 8}$$

With the initial condition $v_1 = 0$ at $r = r_{init}$, this has the solution

$$v_1 = -r\left[1 - \left(\frac{r_{init}}{r}\right)^2\right]. \tag{A 9}$$

In particular, at the nose

$$v_1(r = r_N) = -r_N(t)\left[1 - \left(\frac{1}{r_N(t)}\right)^2\right]. \tag{A 10}$$

REFERENCES

Anderson, D. A., Tannehill, J. C. & Pletcher, R. M. 1984 *Computational Fluid Mechanics and Heat Transfer*. Hemisphere, NY.

Benjamin, T. 1968 Gravity currents and related phenomena. *J. Fluid Mech.* **31**, 209–248.

Bonnecaze, R. T., Huppert, H. E. & Lister, J. R. 1993 Particle-driven gravity currents. *J. Fluid Mech.* **250**, 339–369.

Choboter, P. F. & Swaters, G. E. 2000 On the baroclinic instability of axisymmetric rotating gravity currents with bottom slope. *J. Fluid Mech.* **408**, 149–177.

Csanady, G. T. 1979 The birth and death of a warm core ring. *J. Geophys. Res.* **84**, 777–780.

Dewar, W. & Killworth, P. 1990 On the cylinder collapse problem: mixing and merger of isolated eddies. *J. Phys. Oceanogr.* **20**, 1563–75.

Flierl, G. R. 1979 A simple model for the structure of warm and cold core rings. *J. Geophys. Res.* **84**, 781–785.

Griffiths, R. W. & Linden, P. 1981 The stability of vortices in a rotating, stratified fluid. *J. Fluid Mech.* **105**, 283–316.

Hallworth, M. A., Huppert, H. E. & Ungarish, M. 2001 Axisymmetric gravity currents in a rotating system: experimental and numerical investigations. *J. Fluid Mech.* **447**, 1–29.

Holford, J. M. 1994 The evolution of a front. PhD thesis, University of Cambridge.

Huppert, H. E. & Simpson, J. E. 1980 The slumping of gravity currents. *J. Fluid Mech.* **99**, 785–799.

Killworth, P. 1992 The time-dependent collapse of a rotating fluid cylinder. *J. Phys. Oceanogr.* **22**, 390–397.

Klemp, J. B., Rotunno, R. & Skamarock, W. C. 1994 On the dynamics of gravity currents in a channel. *J. Fluid Mech.* **269**, 169–198.

Nof, D. & Simon, L. M. 1987. Laboratory experiments on the merging of nonlinear anticyclonic eddies. *J. Phys. Oceanogr.* **17**, 343–357.

Press, W. H., Teukolski, S. A. Vetterling, W. T. & Flannery, B. P. 1992 *Numerical Recipes in Fortran*. Cambridge University Press.

Rottman, J. & Simpson, J. 1983 Gravity currents produced by instantaneous release of a heavy fluid in a rectangular channel. *J. Fluid Mech.* **135**, 95–110.

Rubino, A., Hessner, K. & Brandt, P. 2002 Decay of stable warm-core eddies in a layered frontal model. *J. Phys. Oceanogr.* **32**, 188–202.

Ungarish, M. & Huppert, H. 1998 The effects of rotation on axisymmetric particle-driven gravity currents. *J. Fluid Mech.* **362**, 17–51.

Ungarish, M. & Huppert, H. E. 1999 Simple models of Coriolis-influenced axisymmetric particle-driven gravity currents. *Intl J. Multiphase Flow* **25**, 715–737.

Ungarish, M. & Zemach, T. 2003 On the slumping of high Reynolds number gravity currents in two-dimensional and axisymmetric configurations. *Submitted*.

Zemach, T. 2002 Gravity currents: two-layer and asymptotic extensions. Master's thesis, Technion, Haifa, Israel.